Physics of Fluids

Effect of surfactants on jet break-up in drop-on-demand inkjet printing

Cite as: Phys. Fluids **33**, 072112 (2021); https://doi.org/10.1063/5.0056803
Submitted: 14 May 2021 • Accepted: 29 June 2021 • Published Online: 23 July 2021

E. Antonopoulou, O. G. Harlen, M. Rump, et al.

COLLECTIONS

This paper was selected as Featured

This paper was selected as Scilight

View Online Export Citation CrossMark

ARTICLES YOU MAY BE INTERESTED IN

Surfactants influence jetting dynamics and drop formation in inkjet printing
Scilight **2021**, 301110 (2021); https://doi.org/10.1063/10.0005803

Experimental study of the parameters for stable drop-on-demand inkjet performance
Physics of Fluids **31**, 032004 (2019); https://doi.org/10.1063/1.5085868

Maximal spreading of droplet during collision on particle: Effects of liquid viscosity and surface curvature
Physics of Fluids **33**, 083310 (2021); https://doi.org/10.1063/5.0058816

APL Machine Learning
Open, quality research for the networking communities
Now Open for Submissions
LEARN MORE

© 2021 Author(s).

Physics of Fluids ARTICLE scitation.org/journal/phf

Effect of surfactants on jet break-up in drop-on-demand inkjet printing

Cite as: Phys. Fluids 33, 072112 (2021); doi: 10.1063/5.0056803
Submitted: 14 May 2021 · Accepted: 29 June 2021 ·
Published Online: 23 July 2021

View Online Export Citation CrossMark

E. Antonopoulou,[1,2,a)] O. G. Harlen,[3] M. Rump,[4] T. Segers,[5] and M. A. Walkley[6]

AFFILIATIONS

[1]EPSRC Centre for Doctoral Training in Fluid Dynamics, University of Leeds, Leeds LS2 9JT, United Kingdom
[2]Mathematical Institute, University of Oxford, Woodstock Road, Oxford OX2 6GG, United Kingdom
[3]School of Mathematics, University of Leeds, Leeds LS2 9JT, United Kingdom
[4]Physics of Fluids Group, MESA+ Institute for Nanotechnology and MIRA Institute for Biomedical Technology and Technical Medicine, University of Twente, P. O. Box 217, 7500 AE Enschede, The Netherlands
[5]BIOS Lab on a Chip group, Physics of Fluids group, Max-Planck Center Twente for Complex Fluid Dynamics, MESA+ Institute for Nanotechnology, University of Twente, P.O. Box 217, 7500 AE Enschede, The Netherlands
[6]School of Computing, University of Leeds, Leeds LS2 9JT, United Kingdom

[a)]Author to whom correspondence should be addressed: antonopoulou@maths.ox.ac.uk

ABSTRACT

Jet formation and break-up in inkjet printing has been studied and understood mainly for pure liquids. Questions remain as to the role of surfactants on the inkjet printing process at the microsecond timescale. Here, numerical and experimental results demonstrating the effects of surfactants on jet break-up and drop formation at the scales relevant to drop-on-demand inkjet printing are presented. The rapid expansion of the free surface during the fast jetting process results in a depletion of surfactants along the air–liquid interface, resulting in surface tension gradients. During ejection, surfactants are concentrated toward the head of the droplet, while the trailing ligament is found to be almost devoid of surfactants. As a consequence, the initial evolution and pinch-off of the jet from the nozzle are found to be very similar to that of pure water, even though the equilibrium surface tension of the surfactant solution is lower by a factor of two. However, particularly for strong surfactants, Marangoni forces arising from surface tension gradients between the head drop and the ligament are found to delay and can even prevent the break-up of the main drop from the ligament thereby inhibiting the formation of satellite drops.

© 2021 Author(s). All article content, except where otherwise noted, is licensed under a Creative Commons Attribution (CC BY) license (http://creativecommons.org/licenses/by/4.0/). https://doi.org/10.1063/5.0056803

I. INTRODUCTION

A surface active agent or *surfactant* is a molecule, which is characterized by its tendency to absorb at surfaces and interfaces. Surfactants are amphiphilic, meaning that they consist of at least two parts: a part that is soluble in water, the lyophilic or hydrophilic part, and an insoluble lyophobic, or hydrophobic, part.[1] These regions of opposing affinity to water are often referred to as the head- and the tail-group, due to the shape of the molecule. At sufficiently high concentrations, i.e., concentrations above the critical micelle concentration (CMC), surfactants aggregate into micelles in which the hydrophobic group is directed toward the interior of the cluster[2] thereby shielding the hydrophobic group from the water and so reducing the free energy of the system.

Surfactants are commonly used in product formulations. Their versatility makes them very useful in diverse products such as motor oils, pharmaceutical products, laundry detergents and other house cleaning products, drilling muds, and the flotation agents used in beneficiation of ores. Surfactants influence film thicknesses in coating flows,[3–5] the dispersion of surface waves,[6] the dynamics and thicknesses of spreading films,[7,8] and the lifetime of bubbles,[9] foams and emulsions.[10] In recent decades, the applications of surfactants have been extended to high-technology areas such as electronic printing, biotechnology, micro-electronics, and viral research.[11]

A. Surfactants and break-up

Previous studies have looked at the effect of surfactants in a range of different flow geometries, including drop deformation,[12–15] liquid bridges and threads,[16–18] filaments,[19,20] repeated thread formation,[19,21] thin film flows,[22] and the pinch-off dynamics of continuous jets.[23–25] Recent work on the break-up for liquid filaments by recent studies[26,27]

© Author(s) 2021

showed the importance of surfactants in the break-up behavior, especially around the neck region of break-up. However, despite some similarities, there are particular features of drop formation in drop-on-demand inkjet printing that make this problem quite distinct from those previously considered. First, the length scales and timescales are quite different. The inkjet printing process is characterized by length and timescales of micrometers and microseconds, respectively. As a consequence, the transport of the surfactant is dominated by the surface velocity and its modification by the Marangoni stresses with the effects of surface diffusion and bulk exchange being negligible for inkjet printing. Second, most previous studies start from an initial condition of a uniformly covered filament or droplet where the surface concentration has had sufficient time to equilibrate, whereas in inkjet printing, the rapid generation of new surface leads to a surfactant distribution that is far from equilibrium.

In order to investigate the effects of surfactants on inkjet drop formation, we have performed numerical simulations to solve the coupled problems for the fluid dynamics and surfactant transport during jet break-up and drop formation. The mathematical model and the method of numerical solution, using a moving grid finite element method, are discussed in Secs. II and III, respectively. These simulations are compared with experimental observations, described in Sec. IV. We then use the simulations to look in greater detail at the effects of surfactant strength on the jetting dynamics and drop formation presented in Sec. V.

B. Surfactants and surface tension

The surface tension of the water–air interface is high (0.072 $\mathrm{N{\cdot}m^{-1}}$) compared to that of organic solvents, and therefore, surfactants are added to aqueous inks to reduce their surface tension and allow for jetting of aqueous inks. The addition of most common surfactants, like Surfynol 465, Triton X-100 and Dynol, reduces the equilibrium surface tension down to around 0.035 $\mathrm{N{\cdot}m^{-1}}$.[28,29]

Surfactant molecules preferentially migrate to the surface thereby lowering the free-energy associated with the surface, setting up an equilibrium between the surface concentration Γ and bulk concentration c_b of the surfactant. The relationship between Γ and c_b is complex due to the effects of crowding and the formation of micelles. At very low concentrations, Γ is proportional to c_b as the surfactant molecules in the bulk are in monomeric form, and there is plenty of room at the free surface. However, as the surface becomes covered with the surfactant, the rate of increase in Γ with c_b decreases, until a maximum surface concentration Γ_∞ is achieved. This effect is captured empirically by the commonly used Langmuir isotherm,[30,31] given by:

$$\Gamma = \frac{\Gamma_\infty c_b}{c_b + a}, \tag{1}$$

where Γ_∞ is the maximum surface concentration of the surfactant (mol $\mathrm{cm^{-2}}$), c_b is the surfactant concentration in the bulk (mol $\mathrm{l^{-1}}$), a is a constant $[= 55.3 \exp(\Delta G^\circ / \mathscr{R}T)]$ (mol $\mathrm{l^{-1}}$), with ΔG° the free energy of adsorption at infinite dilution, $\mathscr{R}$ is the gas constant, and T is the absolute temperature. This, in combination with the Gibbs equation, gives the Langmuir–Frumkin surface equation of state[32]

$$\gamma = \gamma_p + \mathscr{R}T\Gamma_\infty \ln\left(1 - \frac{\Gamma}{\Gamma_\infty}\right), \tag{2}$$

where γ_p is the pure solvent surface tension (clean interface), $\mathscr{R}$ is the gas constant 8.134 J $\mathrm{mol^{-1}\ K^{-1}}$, and T is the absolute temperature (K), which we will use to relate surface surfactant concentration to surface tension.

However, drop formation from an inkjet nozzle occurs on a timescale of typically 100 μs (Refs. 33–35), which is faster than the time required for the surfactant molecules to reach an equilibrium distribution.[36] As a consequence, the surface tension of the ink–air interface during droplet formation can differ markedly from its equilibrium value. This property is often referred to as the *dynamic surface tension* and is a result of the transient adsorption and distribution of surfactant molecules on the interface. Gradients of surfactant concentration lead to gradients in surface tension that in turn drive flows on the surface, called *Marangoni flows*.[37] There are a variety of methods for measuring dynamic surface tension at liquid–liquid or liquid–gas interfaces;[38] however, these are generally unsuitable for inkjet printing applications, because they are restricted to measuring changes on timescales greater than 1 ms.[39] For example, the growing-drop method[40] relies on simultaneously measuring the pressure, $p(t)$, inside and the radius, $R(t)$, of a drop that is grown at the tip of a capillary tube. This method uses the Young–Laplace equation, $p(t) = 2\gamma(t)/R(t)$, and can only measure surface tension, γ, on the timescale of milliseconds. The timescale for the surface surfactant concentration to reach equilibrium can be estimated from the diffusion-limited transport of surfactants from the solution onto a planar interface.[17,18,41] The characteristic timescale for transport via diffusion is given by,

$$\tau_D = \frac{h_p^2}{D}, \tag{3}$$

where D is the diffusion coefficient for the surfactant molecules (typically around $3 \times 10^{-10}\ \mathrm{m^2\ s^{-1}}$)[42] and h_p is the depletion depth given by:

$$h_p = \frac{\Gamma_{\mathrm{eq}}}{c_b}, \tag{4}$$

where Γ_{eq} is the equilibrium surface concentration of the surfactant (mol $\mathrm{cm^{-2}}$). The depletion depth varies with the solubility and concentration of the surfactant.

In our experiments, we used Triton X-100 as the surfactant. The conditions of the experiments correspond to the parameters:[43]

$$D \approx 2.6 \times 10^{-10}\ \mathrm{m^2\ s^{-1}},$$
$$\Gamma_{\mathrm{eq}} = 2.9 \times 10^{-6}\ \mathrm{mol\ m^{-2}},$$
$$c_b = 0.22\ \mathrm{mol\ m^{-3}}.$$

These give an estimated depletion depth of $h_p = 13\ \mu$m, which is half the jet diameter (25 μm), and an estimated diffusion time of around 0.5 s, a factor 3×10^3 longer than the break-off time observed in our experiments. Moreover, this timescale is based on the assumption of a planar interface, and the diffusion time will be slower if the curvature of the surface is included. Therefore, we can conclude that bulk exchange is negligible on the timescales of interest.

II. GOVERNING EQUATIONS

A. Problem definition

In order to examine the effects of surfactants on jet break-up, we simulate the evolution of a surfactant solution ejected by a drop-on-

© Author(s) 2021

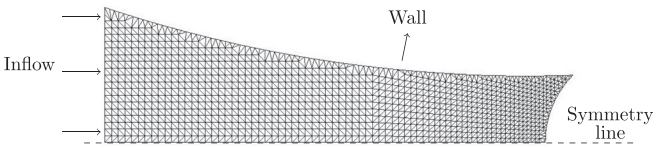


FIG. 1. Nozzle shape and initial mesh used in the simulations. The jet is assumed to be axisymmetric, so for the production of subsequent images, the results are mirrored around the axis of symmetry.

demand printhead. We will not model the detailed flow within the entire printhead, but consider only the flow in the region close to the nozzle. Since the nozzle is axisymmetric this allows us to make the assumption of axisymmetry where the axis of symmetry lies at the center of the nozzle, even though the printhead itself is non-axisymmetric. The shape of the nozzle was chosen to replicate the dimensions of the experimental nozzle, which has a radius of 25 μm. The fluid used has the viscosity and density of water, jetted with a droplet speed of 4 m s^{-1}. The initial finite-element grid is shown in Fig. 1.

As we are not directly modeling the piezo-electric acoustic drive, we impose a time-dependent flow velocity at the inlet boundary (left side of Fig. 1) to replicate the mass flow driven by the pressure variations within the print-head. This flow is chosen to have a Poiseuille profile with a time-dependent amplitude chosen so that the position of the meniscus within the nozzle approximately matches the experimental observations and has a "pull–push–pull" waveform. This is composed of three segments. In the first segment, the meniscus is drawn back into the print-head. In the second segment, the velocity reverses and drives liquid from the reservoir through the nozzle orifice. In the final segment, liquid is again drawn back into the nozzle from the tail of the emergent jet. A graph of the time dependence of the signal used in the simulations and the corresponding position of the free surface is shown in Fig. 2, where amplitude has been non-dimensionalized by the maximum value of the push phase and time by the Rayleigh or

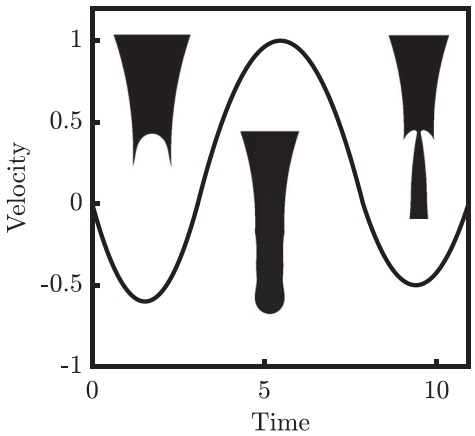


FIG. 2. Plot of the dimensionless driving signal as a function of dimensionless time, which is imposed as a flux boundary condition over the nozzle inlet. The velocity has been non-dimensionalised by its maximum value. This jetting speed was set to 5.5 m s^{-1} to match the experiments. Images show the meniscus position at each stage of the pull–push–pull waveform.

capillary timescale $t_R = \sqrt{\rho R^3/\gamma_p} \sim 15$ μs. By dividing this volume flow by the cross-sectional area of the nozzle exit, we can define a jetting speed based on the flow rate at the maximum amplitude. For the fluid properties corresponding to the experiments, a droplet speed of 4 m s^{-1} requires a jetting speed of 5.5 m s^{-1}. However, as the droplet speed will vary with viscosity and surface tension, we use the jetting speed rather than the droplet speed as the velocity scale. The same waveform was used in all the simulations, meaning that we are neglecting the coupling between the surface tension and the acoustics within the print-head, which will exist in practice.

As the temperature of the fluid in the print-head is maintained at a constant value, there are no significant temperature variations during the jetting process and hence the viscosity and surface tension can be assumed to be constant. We can also neglect the effects of gravity due to the small scales involved,[44] as the Stokes number $\mathrm{St} = \frac{\rho g R^2}{\mu U}$ is of order of $\mathcal{O}(10^{-5})$. Here, g is the gravitational acceleration, U is the jetting speed defined above, R is the drop radius, and μ is the dynamic viscosity of the fluid. Hence, the dynamics are described by,

$$\rho \frac{\mathrm{D}\boldsymbol{u}}{\mathrm{D}t} = \nabla \cdot \boldsymbol{\sigma}, \tag{5}$$

where the Newtonian stress tensor $\boldsymbol{\sigma}$ is given by

$$\boldsymbol{\sigma} = -p\mathbf{I} + \mu\left[\nabla \boldsymbol{u} + (\nabla \boldsymbol{u})^T\right], \tag{6}$$

where $\boldsymbol{u}$ is the fluid velocity and p is the pressure in the fluid, together with the condition of incompressibility,

$$\nabla \cdot \boldsymbol{u} = 0. \tag{7}$$

We assume that the contact line is pinned at the nozzle outlet and that no-slip occurs at the nozzle walls, where conditions of zero velocity are imposed ($\boldsymbol{u} = 0$). At the free surface, we assume that the drag on a droplet due to air resistance is negligible[45] and impose a boundary condition on the stress due to surface curvature,

$$[\boldsymbol{\sigma} \cdot \boldsymbol{n}]^{\mathrm{jet}}_{\mathrm{air}} = -\gamma(\nabla_s \cdot \boldsymbol{n})\boldsymbol{n} + \nabla_s \gamma. \tag{8}$$

Here, γ is the local coefficient of surface tension, $\boldsymbol{n}$ is the unit vector normal to the free surface (directed outward from the jet), and the surface divergence operator is given by $\nabla_s \cdot := \nabla \cdot (\boldsymbol{I} - \boldsymbol{nn})$. $\nabla_s \cdot \boldsymbol{n}$ is the local curvature of the surface and can be written as

$$\nabla_s \cdot \boldsymbol{n} = \left(\frac{1}{R_1} + \frac{1}{R_2}\right), \tag{9}$$

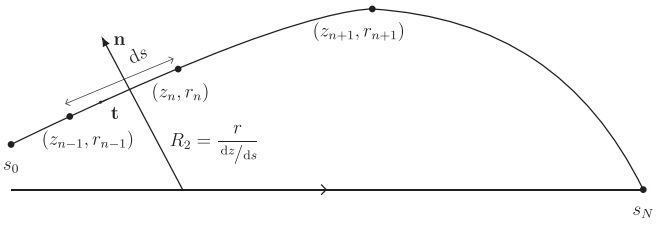


FIG. 3. Free surface and unit vectors, where tangential vector $\boldsymbol{t}$, normal vector $\boldsymbol{n}$ to the surface, radial coordinate r, axial coordinate z, radius of curvature R_2, and s is the contour length of the surface.

© Author(s) 2021

where R_1, R_2 are the principle radii of curvature.[46]

In common with others' studies,[17,18,31] we assume that the surface tension γ and surface surfactant concentration Γ are related by the Langmuir–Frumkin surface equation of state Eq. (2). The surfactant transport on the liquid–gas interface is governed by a time-dependent advection–diffusion equation,[15,47]

$$\frac{\partial \Gamma}{\partial t} + \nabla_s \cdot (\Gamma \boldsymbol{u}) - \mathscr{D}\nabla_s^2 \Gamma = b, \tag{10}$$

where $\Gamma(z,t)$ is the surface concentration of surfactant, $\mathscr{D}$ is the surfactant surface diffusivity ($m^2\ s^{-1}$), ∇_s is the vector differential operator on the surface, and b is the net exchange of surfactants with the bulk, which we assume to be zero.

B. Non-dimensional equations

The equations can be put into dimensionless form by scaling length with the nozzle outlet radius R_N, velocities by the jetting speed U and pressure, and stress by ρU^2. This rescaling yields the dimensionless governing equations (5) and (7), for the fluid domain Ω, as follows:

$$\frac{\mathrm{D}\boldsymbol{u}}{\mathrm{D}t} - \nabla \cdot \boldsymbol{\sigma} = 0, \tag{11}$$

$$\nabla \cdot \boldsymbol{u} = 0. \tag{12}$$

Note that we use non-dimensional quantities from now on without changing the notation; therefore, t, $\boldsymbol{u}$, p, and $\boldsymbol{\sigma}$ are now the dimensionless time, velocity, pressure, and stress, respectively, with the stress tensor Eq. (6) given by

$$\boldsymbol{\sigma} = -p\boldsymbol{I} + \frac{1}{Re}\left[\nabla \boldsymbol{u} + (\nabla \boldsymbol{u})^T\right]. \tag{13}$$

The dimensionless interface boundary condition Eq. (8) on the free surface S is given by

$$[\boldsymbol{\sigma} \cdot \boldsymbol{n}]_{\text{air}}^{\text{jet}} = -\frac{\gamma}{We}(\nabla_s \cdot \boldsymbol{n})\boldsymbol{n} + \frac{1}{We}\nabla_s \gamma. \tag{14}$$

Here, Re and We are the Reynolds and Weber numbers,

$$Re = \frac{\rho U R_N}{\mu},$$

$$We = \frac{\rho U^2 R_N}{\gamma_p},$$

and the surface tension γ is defined relative to its value for the pure solvent in the form

$$\gamma = 1 + \beta \ln(1 - KC), \tag{15}$$

where the parameter

$$\beta = \frac{\Gamma_\infty RT}{\gamma_p}, \tag{16}$$

provides a measure for the strength of the surfactant, and the surfactant concentration is non-dimensionalized by the equilibrium surface surfactant concentration Γ_{eq} (at the given surfactant bulk concentration of the solution) as

$$C = \frac{\Gamma}{\Gamma_{\text{eq}}}. \tag{17}$$

This introduces an additional non-dimensional parameter

$$K = \frac{\Gamma_{\text{eq}}}{\Gamma_\infty}, \tag{18}$$

which represents the ratio of the equilibrium surfactant concentration on the surface to the maximum surface concentration for the given surfactant.

The dimensionless surfactant transport equation (10) is

$$\frac{\mathrm{D}_s C}{\mathrm{D}_s t} - \frac{1}{Pe}\nabla_s^2 C = B, \tag{19}$$

where $\boldsymbol{x}$ and t are now in dimensionless form, B is the dimensionless bulk exchange rate, and Pe is the surface Péclet number given by

$$Pe = \frac{R_N U}{\mathscr{D}}, \tag{20}$$

which determines the importance of convection of the surfactant molecules relative to its diffusion along the free surface. Here, $\frac{\mathrm{D}_s}{\mathrm{D}_s t}$ is defined as the surface Lagrangian derivative

$$\frac{\mathrm{D}_s f}{\mathrm{D}_s t} = \frac{\partial f}{\partial t} + \nabla_s \cdot (\boldsymbol{u} f),$$

and includes the effects of surface dilation as well as advection.

III. LAGRANGIAN FINITE ELEMENT METHOD

The fluid equations were solved using the Lagrangian finite element method.[35] A key property of the Lagrangian finite element scheme is that the nodes move with the fluid velocity,[48] so that the dilation and advection on the surface are handled by the motion of the nodes.

A. Weak formulation

We discretize Eqs. (11) and (12) in space using the finite element method.[49] We define ϕ_i and ψ_j as basis functions for the velocity and pressure finite element spaces, respectively, which here are chosen to be linear $P1$ functions over triangular elements. To develop the finite element approximation, we obtain the weak formulation of the equations by multiplying each of the components of the momentum equation (11) with ϕ_i and Eq. (12) with ψ_j and integrating over the spatial domain Ω.

Application of the surface divergence theorem[50] gives

$$\int_\Omega \phi_i \frac{\mathrm{D}\boldsymbol{u}}{\mathrm{D}t}\mathrm{d}\Omega + \int_\Omega \nabla \phi_i \cdot \boldsymbol{\sigma}\mathrm{d}\Omega = \int_S \phi_i \boldsymbol{\sigma} \cdot \boldsymbol{n}\mathrm{d}S, \quad i = 1, \ldots, N_u, \tag{21}$$

$$\int_\Omega \psi_j (\nabla \cdot \boldsymbol{u})\mathrm{d}\Omega = 0, \quad j = 1, \ldots, N_p, \tag{22}$$

where S is the boundary of the domain Ω and N_u and N_p are the number of non-Dirichlet velocity and pressure nodes, respectively.

B. Finite element formulation for dynamic surface tension

The jet is assumed to be axisymmetric, so that within a radial slice the tangential and normal vectors, $\boldsymbol{t}$ and $\boldsymbol{n}$, respectively, are given in cylindrical polar coordinates by (Fig. 3):

© Author(s) 2021

$$\boldsymbol{t} = \left(\frac{\mathrm{d}z}{\mathrm{d}s}, \frac{\mathrm{d}r}{\mathrm{d}s}\right), \tag{23}$$

$$\boldsymbol{n} = \left(\frac{\mathrm{d}r}{\mathrm{d}s}, -\frac{\mathrm{d}z}{\mathrm{d}s}\right). \tag{24}$$

The surface curvature is given by[35]

$$(\nabla_s \cdot \boldsymbol{n})\boldsymbol{n} = -\frac{\mathrm{d}\boldsymbol{t}}{\mathrm{d}s} + \frac{\boldsymbol{n}}{R_2}.$$

Hence, Eq. (14) can be rewritten as

$$[\boldsymbol{n}\cdot\boldsymbol{\sigma}]_{\text{surface}} = \frac{1}{We}\left(\gamma\frac{\mathrm{d}\boldsymbol{t}}{\mathrm{d}s} - \frac{\boldsymbol{n}}{R_2} + \boldsymbol{t}\frac{\mathrm{d}\gamma}{\mathrm{d}s}\right) = \frac{1}{We}\left[\frac{\mathrm{d}}{\mathrm{d}s}(\gamma\boldsymbol{t}) - \gamma\frac{\boldsymbol{n}}{R_2}\right]. \tag{25}$$

Note that Eq. (25) also contains the constant surface tension case. Thus, for an axisymmetric geometry, after integration by parts, the right-hand side of Eq. (21) becomes

$$\begin{aligned}\int_S (\boldsymbol{n}\cdot\boldsymbol{\sigma})\phi_i r\mathrm{d}s\mathrm{d}\theta &= -\frac{2\pi}{We}\left(\int_{s_0}^{s_N}\gamma\frac{\boldsymbol{n}}{R_2}r\phi_n\mathrm{d}s - \int_{s_0}^{s_N}\frac{\mathrm{d}}{\mathrm{d}s}(\gamma\boldsymbol{t})\phi_i r\mathrm{d}s\right)\\ &= -\frac{2\pi}{We}\left(\int_{s_0}^{s_N}\gamma\frac{\mathrm{d}z}{\mathrm{d}s}\boldsymbol{n}\phi_i\mathrm{d}s + \int_{s_0}^{s_N}\gamma\boldsymbol{t}\frac{\mathrm{d}}{\mathrm{d}s}(r\phi_i)\mathrm{d}s\right.\\ &\quad\left. - [\gamma\boldsymbol{t}r\phi_i]_{s_0}^{s_N}\right),\end{aligned} \tag{26}$$

where s_0, s_N are the beginning and end points of the free surface. Note that the contribution from the end points is zero in our case as the point s_0 is part of the nozzle boundary so that ϕ_i is zero there for all velocity unknowns, and the other end s_N is located on the axis so that $r = 0$.

The integration by parts removes the derivative of the surface tension, so that the integrals in Eq. (26) are the same as in the constant surface tension case, described in Refs. 35 and 51. For points on the surface, ϕ_n is non-zero only on the two edges connected to point n. Therefore, for the case of linear basis functions ϕ_n, where $\frac{r}{R_2} = \frac{\mathrm{d}z}{\mathrm{d}s}$ and $\gamma\boldsymbol{n}$ are constant on each edge the integrals can be performed analytically, so that surface force contribution Eq. (14) from the basis function corresponding to a point (z_n, r_n) on the surface in the weak formulation is given by

$$\begin{aligned}\frac{We}{2\pi}\int_S (\boldsymbol{n}\cdot\boldsymbol{\sigma})\phi_n r\mathrm{d}s\mathrm{d}\theta &= -\frac{1}{2}(\gamma_-\boldsymbol{n}_-\Delta z_- + \gamma_+\boldsymbol{n}_+\Delta z_+)\\ &\quad + r_n(\gamma_+\boldsymbol{t}_+ - \gamma_-\boldsymbol{t}_-),\end{aligned} \tag{27}$$

where $\Delta z_- = z_n - z_{n-1}$, $\Delta z_+ = z_{n+1} - \Delta z_n$, and $\gamma_{-,+}$ is the surface tension on edges connected to point n.

C. Time discretization

In the Lagrangian frame, the Lagrangian material derivative $\mathrm{D}\boldsymbol{u}/\mathrm{D}t$ becomes the ordinary time derivative $\mathrm{d}\boldsymbol{u}/\mathrm{d}t$. Time derivatives are discretized using a θ scheme where the value of a variable ψ at the $(n+1)$th time step is given by

$$\psi_{n+1} = \psi_n + \delta t\left[\theta\dot{\psi}_{n+1} + (1-\theta)\dot{\psi}_n\right], \tag{28}$$

where δt is the time step, $\theta \in [0, 1]$ is the weighting parameter of the scheme, and $\dot{\psi} = \mathrm{d}\psi/\mathrm{d}t$. The size of the time step δt is restricted by a CFL condition of the form $U\delta t < \delta x$, due to the moving mesh, where U is a typical flow velocity and δx is a typical element size.

In addition to the time derivative in the momentum equation, the solution at the $(n+1)$th step depends upon the position of the nodes, which move with the fluid velocity. For each variable ψ, Eq. (28) results in a non-linear algebraic equation for ψ_{n+1} in terms of ψ_n. We linearize this equation via a Picard iteration scheme, since the node positions depend on the solution for the velocity.

The position $\boldsymbol{x}$ of any mesh node (except those on the nozzle inlet boundary) is updated after each time step as

$$\boldsymbol{x}_{n+1} = \boldsymbol{x}_n + \delta t[\theta\boldsymbol{u}_{n+1} + (1-\theta)\boldsymbol{u}_n], \tag{29}$$

where θ is the same parameter as in Eq. (28). For the nodes on the nozzle inlet, special consideration is taken. Their positions are held constant to preserve the nozzle shape and the applicability of the driving boundary condition. This algorithm is presented in Ref. 44 in more detail.

D. Surfactant transport

To calculate the evolution of the surfactant concentration, we exploit the Lagrangian properties of the surface edges of the finite elements, which means that advection does not change the number of surfactants on the surface corresponding to the edge between two nodes (z_1, r_1) and (z_2, r_2). Hence defining

$$2\pi N = \int_A C\mathrm{d}A,$$

as the number of surfactant molecules on the edge, the evolution of the surfactant distribution is given by

$$\frac{\mathrm{d}N}{\mathrm{d}t} + J_2 - J_1 = B, \tag{30}$$

where

$$J_i = -\frac{r_i}{Pe}\frac{\partial C}{\partial s}\bigg|_{(z_i, r_i)} \tag{31}$$

and

$$2\pi B = \int_A b\mathrm{d}A.$$

In the absence of bulk exchange, so that $B = 0$ in Eq. (30), the number of surfactants on an edge $N = CA$ changes only as a result of the diffusive flux between edges, given by Eq. (31), which we calculate as

$$J = -\frac{2r}{Pe}\left[\frac{N_+/A_+ - N_-/A_-}{S_+ - S_-}\right], \tag{32}$$

where $N_\pm$, $A_\pm$, and $S_\pm$ are, respectively, the surfactant number, area, and midpoint of the adjoining edges. The initial condition is chosen such that the initial surfactant number on each edge corresponds to the equilibrium concentration, so that $C = 1$.

© Author(s) 2021

E. Maximum packing concentration and surfactant transport

Although overall the jetting process leads to a dilation of the free surface and hence a reduction in surfactant concentration, locally there are areas where the surface area is contracting. Where this occurs it is possible for the local concentration to exceed the maximum packing concentration Γ_∞, which in Eq. (1) would lead to the unphysical situation of the surface tension becoming zero. In reality, strong repulsive forces between the surfactant molecules would prevent this from happening. The monolayer will buckle when the maximum packing is reached. The maximum packing and corresponding minimum surface tension depend on the type of surfactant. For phospholipid monolayers, the surface tension can reach zero,[52] but not in the case here.

As this only happens in very small regions, rather than adjusting the surfactant transport, we modify the equation-of-state to

$$\gamma = \max(1 + \beta \ln(1 - KC), \gamma_{\min}), \tag{33}$$

where $\gamma_{\min}$ is the minimum surface tension that can be achieved for this surfactant. As noted earlier, the addition of commonly used surfactants reduces the surface tension of water from 0.072 N·m^{-1} to around 0.035 N·m^{-1} at the CMC but further increase in the bulk surfactant concentration does not lower the surface tension further. Therefore, in the simulations, we set $\gamma_{\min} = 0.49$. This modified equation of state is shown in Fig. 4, where we see that the minimum surface tension of 0.035 N·m^{-1} is reached at lower concentrations for higher β.

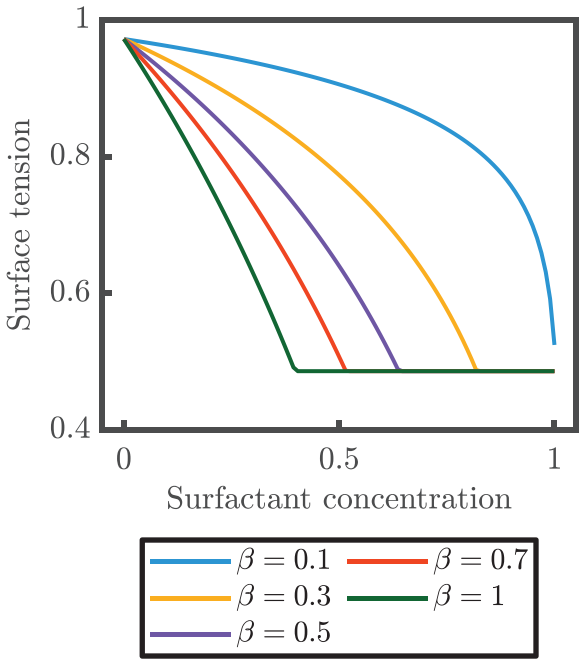


FIG. 4. Surface tension as a function of surfactant concentration using Eq. (33) for different surfactant strengths β. A minimum surface tension equal to the equilibrium surface tension is imposed at the value of 0.035 N m^{-1}.

F. Resolution and accuracy

In order to test the implementation of the algorithm, the results for $\beta = 0$ were compared with those presented in Ref. 35 and were found to give identical results for the same mesh and time step. To test the effect of the spatial resolution on the accuracy of the calculations, we performed simulations with three different mesh resolutions. Comparison between the results for the reference mesh used for this study and the highest resolution mesh gives an error of less than 2% in the calculated drop speed and no differences in the qualitative break-up behavior. This implies that the mesh used is sufficiently fine to capture the dynamics.

IV. EXPERIMENTAL DETAILS

The model was compared to experiments performed at room temperature on a 50 μm diameter single nozzle printhead (AD K-501 and AD-H-501, Microdrop Technologies GmbH). Aqueous surfactant solutions were supplied from a rubber-free plastic syringe to the printhead via flexible PEEK tubing (Upchurch Scientific). Before the jetting experiments, the meniscus was positioned at the nozzle exit by manually adjusting the piston of the syringe. The printhead was driven by a rectangular waveform with a width of 30 μs and a rise and fall time of 0.2 μs. The waveform was generated by an arbitrary waveform generator (Agilent 33440A) and amplified to an amplitude of 66.4 V by a broadband amplifier (Falco System WMA-300).

The imaging setup is shown in Fig. 5. The setup consisted of a modular microscope (BXFM-F, BXFM-ILHS, Olympus) equipped with a 5 times magnifying objective (MPLFLN, Olympus) and an additional two times magnifying lens resulting in an effective magnification of 10 times. The microscope was connected to a CCD camera (Lumenera, Lw135 m, 4.65 × 4.65 μm^2 pixels) via a tube lens (U-TLU) resulting in an imaging resolution of 465 nm/pixel. Sufficient illumination was provided via laser-induced fluorescence (iLIF)[53] using a 7 ns laser light flash (Quantel EverGreen, Nd: YAG, $\lambda = 532$ nm, 7 ns) of which the coherence was removed by a fluorescent diffusor (Lavision, Part Nos. 118417 and 1003144). The resulting 8 ns incoherent light flash was condensed onto the imaging plane using a lens (2 cm focal distance) and an optical fiber. The waveform generator, the laser, and the camera were triggered with nanosecond precision using a pulse-delay generator (Berkeley Nucleonics Corp., BNC 575). The pulse delay generator was controlled via custom-made software programed in Labview (National Instruments). To avoid surfactant aggregation due to evaporation at the meniscus and to ensure a uniform surfactant concentration in the bulk liquid behind the meniscus, first, 999 droplets were jetted at a rate of 1000 droplets/s. Subsequently, the jetting process was stopped for 10 ms to allow surfactants to adsorb to the meniscus. After these 10 ms, a next series of 999 droplets was jetted at a frequency of 1000 droplets/s. For each series of 999 droplets, the first droplet was imaged. The imaging software was programed such that the pulse delay generator increased the delay of the light flash with respect to the piezo actuation pulse by 2 μs for every image. In this manner, the droplet formation process was recorded stroboscopically at the extremely short exposure time of 8 ns.

In Figs. 6 and 7, we compare snapshots at the pinch-off from the nozzle and at a later time after the break-off of the head droplet from the ligament for the pure water and the water–Triton X-100 solution. For the Triton-X simulations, we use a value for $\beta = 0.1$ which was estimated using the value of the equilibrium surface tension[28] and

© Author(s) 2021

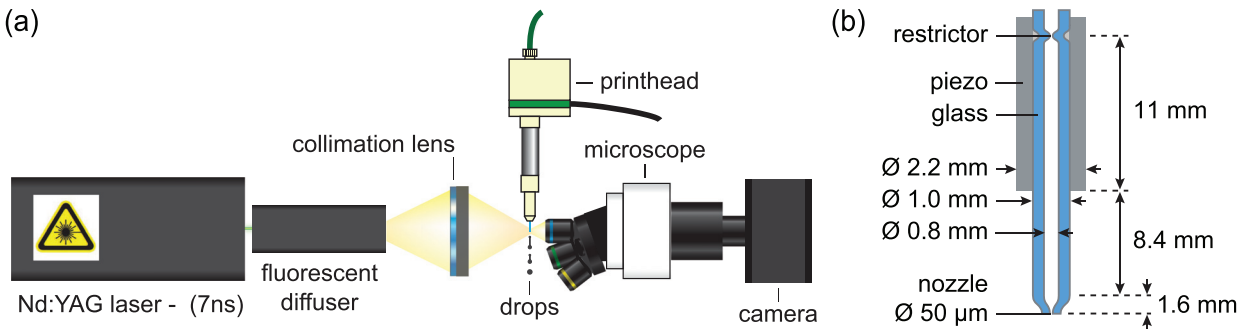


FIG. 5. (a) Schematic of the experimental setup and (b) nozzle specifications.

$K = 1$ since the bulk concentration is at the CMC, which gives a fully covered meniscus at the initial resting stage. The jetting speed in the simulations was set to 5.5 m s^{-1} to match the drop speed of 4 m s^{-1} of the experiments, corresponding to a Reynolds number of 100 and a Weber number of 5.56. We note that here the major uncertainty in the comparison between the simulations and experiment is the precise form of the driving waveform and any effect of the acoustics on the meniscus. Although we can observe some small differences, overall there is good agreement between the experiments and simulations. However, by comparing Figs. 6 and 7, we observe that there is very little difference between the pure water and the water–Triton X-100 solution. The main difference seen in figures (a) is that the neck connecting the main drop to the ligament is thicker for the case of the surfactant solution as the presence of surfactants slightly retards the thinning and break-up of this neck. This difference is also captured in the simulations.

V. RESULTS

The experimental results discussed above show that the jetting of a surfactant solution closely resembles that of pure water, even though the equilibrium surface tension of the solution is half that of water. There are however some subtle differences seen at the point of pinch-off of the main drop. To explore the mechanisms responsible, we use the simulations to investigate how the surfactants are distributed and the form of the resulting Marangoni stresses for different values of the surfactant strength β for an initial concentration $K = 1$, corresponding to a fully covered meniscus interface, using the same drive waveform with $Re = 100$ and $We = 5.56$, giving an Ohnesorge number

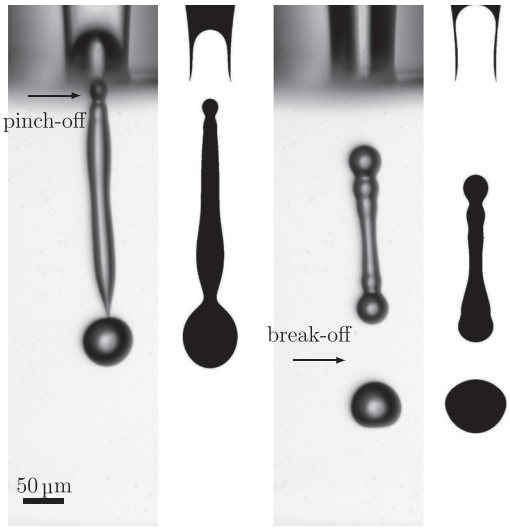


FIG. 6. Comparison between experiments (grey background) and simulations (white background) with water at different times for a simulation jetting speed of 5.5 m s^{-1} giving a droplet speed of 4 m s^{-1} (a) at pinch-off from the nozzle $t = 140$ μs and (b) at break-off of the main droplet from the ligament at $t = 168$ μs.

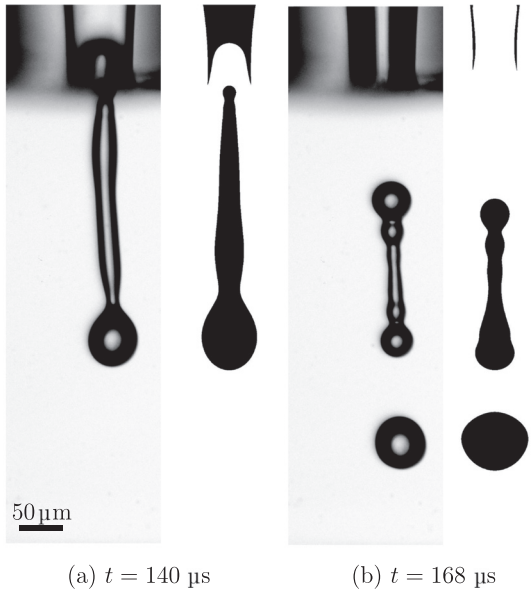


FIG. 7. Comparison between simulations (white background) and experiments (grey background) with water–Triton X-100 mixture at 1 CMC at different times for a simulation jetting speed of 5.5 m s^{-1} giving a droplet speed of 4 m s^{-1} (a) at pinch-off from the nozzle $t = 140$ μs and (b) at break-off of the main droplet from the ligament at $t = 168$ μs.

© Author(s) 2021

$$Oh = \frac{\mu}{\sqrt{\rho\gamma_{eq}R}} = \frac{\sqrt{We}}{Re} = 0.024.$$

A. Surfactant distribution

To show the importance of the Marangoni stress in the surfactant distribution, in Figs. 8 and 9 we compare a weaker surfactant of strength $\beta = 0.1$ with the strong surfactant of strength $\beta = 1$. As the newly formed droplet is pushed out of the nozzle, surfactants are concentrated at the tip of the drop [Fig. 8(a)]. This is a consequence of the pull–push drive. During the first pull stage, a new surface is generated by the retraction of the meniscus into the nozzle lowering the concentration. However, during the subsequent push-out stage, the meniscus initially contracts before expanding again as the fluid is squeezed at the nozzle, which has the effect of transporting the surfactants toward the front of the droplet. As the new surface is created at a rate several orders of magnitude faster than the surfactants can diffuse, diffusion has a negligible effect on the surfactant transport. Therefore, the dominant mechanism controlling the surfactant distribution is the advection by the surface velocity, which is modified by the Marangoni forces.

At the time when the ejected fluid pinches off from the nozzle, Fig. 8(b), there is a clear difference between the cases of strong and weak surfactant: $\beta = 0.1$ has a localized area of high concentration toward the rear of the drop, while $\beta = 1$ has a lower and more uniform concentration along the head. This difference is caused by the stronger Marangoni force for $\beta = 1$ that acts to oppose gradients in surfactant concentration. However in both cases, the trailing ligament is almost entirely surfactant-free.

A similar variation in the distribution can be seen at the time of the capillary break-off in Fig. 9, where for the weak surfactant ($\beta = 0.1$) case there is a localized area of high surfactant concentration, toward the back of the main drop. This results from the advection of the surfactant from the front of the main drop by circulatory flow around the surface of the drop. In comparison, in the case of the stronger surfactant, the concentration is less localized and the maximum located closer to the rear of the droplet. This can also be seen in the top subfigure within Fig. 10 that shows the surfactant concentration along the interface at a time just before the capillary break-off.

After the capillary break-off, when the head droplet has separated from the ligament, the surfactant concentration of the droplet approaches a uniform surfactant concentration, driven by the Marangoni stress and subject to change with the small amplitude oscillations of the droplet, [Fig. 9(b)]. The ligament has a much lower surfactant concentration than the drop, which will also eventually relax to a uniform concentration.

B. Effect of surfactants on thinning and break-up

We now look in more detail at the rates of thinning of the liquid bridges at two break events and compare these to the asymptotic theories for self-similar capillary thinning.[54–56] Previous studies of surfactant covered filaments[16,19,24,57,58] find that as the thread thins, the rapid dilation of the surface in the vicinity of the break-off leads to an almost surfactant-free interface at the break-off point, so that the very

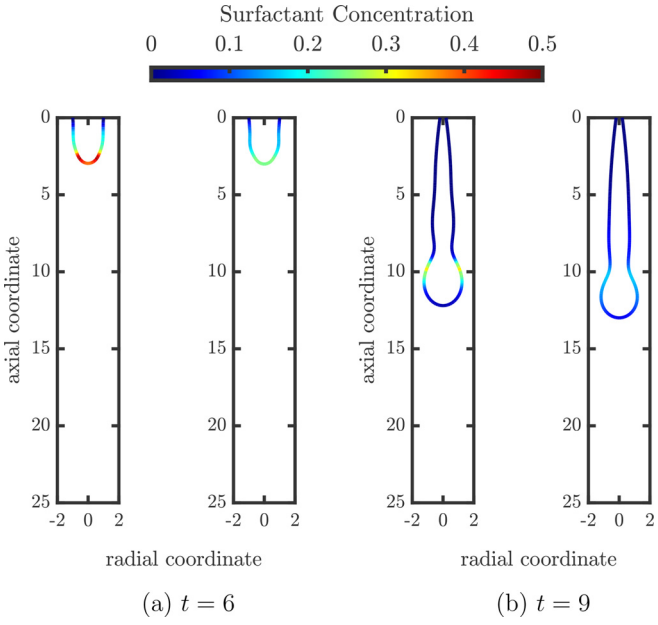


FIG. 8. Surfactant distribution along the interface at different stages of the jetting process for $\beta = 0.1$ on the left and $\beta = 1$ on the right of each subfigure for jetting at $Re = 100$, $We = 5.56$. From left to right: (a) end of push-stage ($t = 6t_R$) and (b) pinch-off from the nozzle ($t = 9t_R$). Here, the color bar limits are the same for both cases. The concentration shown here is non-dimensionalized by the equilibrium concentration.

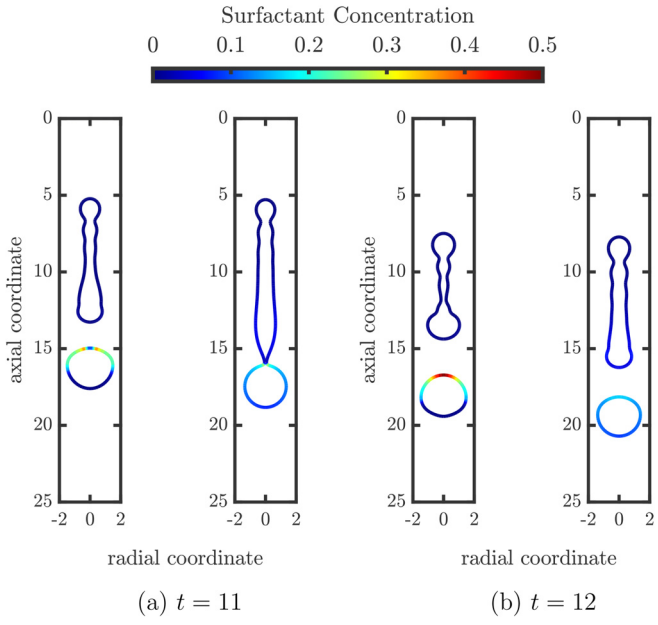


FIG. 9. Surfactant distribution along the interface at different stages of the jetting process for $\beta = 0.1$ on the left and $\beta = 1$ on the right of each subfigure for jetting at $Re = 100$, $We = 5.56$. From left to right: (a) capillary break-off ($t = 11t_R$) and (b) ligament retraction ($t = 12t_R$). Here, the color bar limits are the same for both cases. The concentration shown here is non-dimensionalized by the equilibrium concentration.

© Author(s) 2021

final stages of the dynamics follow the universal thinning law for a surfactant-free interface.[54] However, surfactants do affect the approach to this singularity and in recent studies[26,27] showed that the presence of surfactants can inhibit end-pinching in nearly inviscid filaments as a consequence of the Marangoni stress generated in the region of the neck. At the point of capillary break-off of the droplet from the ligament, there is a gradient in surfactant concentration and hence an associated Marangoni stress. Figure 10 shows the interface shape, the surfactant concentration, the surface tension, and the Marangoni stress,

$$T_M = \boldsymbol{t} \cdot \nabla_s \gamma, \tag{34}$$

just before the main droplet breaks off from the ligament for a strong surfactant ($\beta = 1$). There is a negative spike in T_M near the break-off point meaning that the Marangoni force is pointing away from the main droplet toward the ligament, resisting thinning.

As seen in Figs. 8 and 9, the deformation of the free surface during jetting leads to a lower concentration of surfactant in the ligament compared to that of the main droplet. Therefore, the surface tension is lower in the main droplet compared to the relatively surfactant-free ligament. As a consequence, we find different behaviors in the approach to the two main break events, the pinch-off of the jet from the nozzle and the break-off of the main drop from the ligament.

At the pinch-off of the jet from the nozzle, the surfactant concentration is very low near the rear of the ligament so that the surface tension is close to that of the pure solution. As a consequence, the pinch-off time (Fig. 12) and radius thinning rate remain unchanged from that of the pure fluid.

In our simulations, the Ohnesorge number is small ($Oh = 0.024$), and therefore, we expect to be in the Euler regime for capillary thinning,[56] over the length scale range captured by the simulations. Once the neck radius becomes small compared to the drop radius, the behavior in the vicinity of the neck is locally determined and independent of initial conditions. Therefore, we expect that in the capillary break-off region, the neck radius R is given by

$$R^{3/2} \propto \left(\frac{\gamma}{\rho}\right)^{1/2} \tau, \tag{35}$$

where $\tau = t_b - t$ is the time until break-off. This scaling indicates that the thinning rate should increase with the surface tension as $\gamma^{1/2}$.

For surfactant-free fluids, we have verified that this behavior is found in our simulations for both break-off events. We also find that the thinning rate at the break-off from the nozzle follows the same thinning rate as the pure fluid due to the absence of surfactants. However, the presence of surfactants does affect the thinning rate at the capillary break-off of the head drop.

In all cases, we still find that the radius decreases as $\tau^{2/3}$ but the coefficient of thinning $\kappa = R^{3/2}/\tau$ depends upon the surfactant strength. For values of β up to $\beta = 0.6$, κ decreases linearly with β as shown in Fig. 11. However, above $\beta = 0.6$ the thinning of the neck becomes independent of the surfactant strength. This saturation in the rate of thinning can be explained from the form of the modified

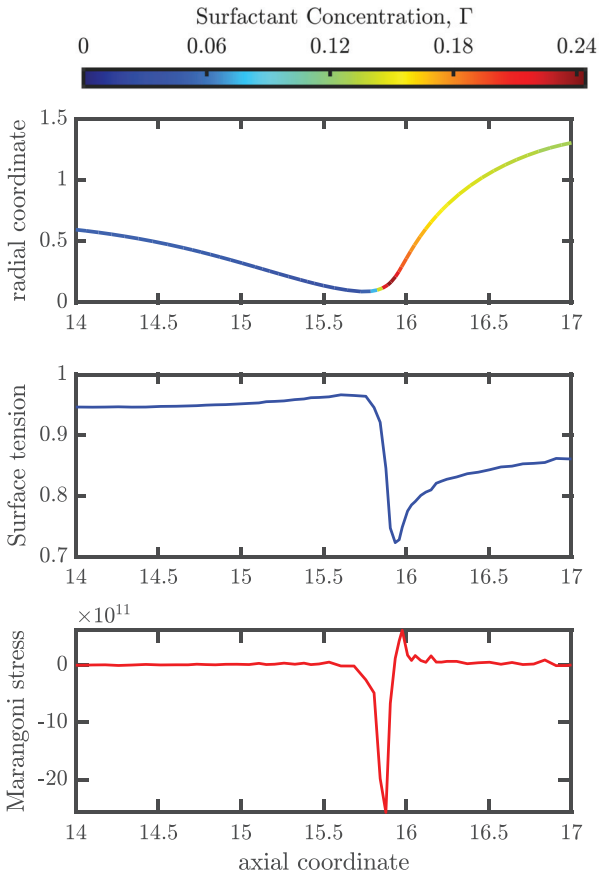


FIG. 10. Surfactant concentration with interface shape, surface tension, and Marangoni stress along the free surface for $\beta = 1$ at $t = 11$, before break-off. The horizontal axis is common for every figure.

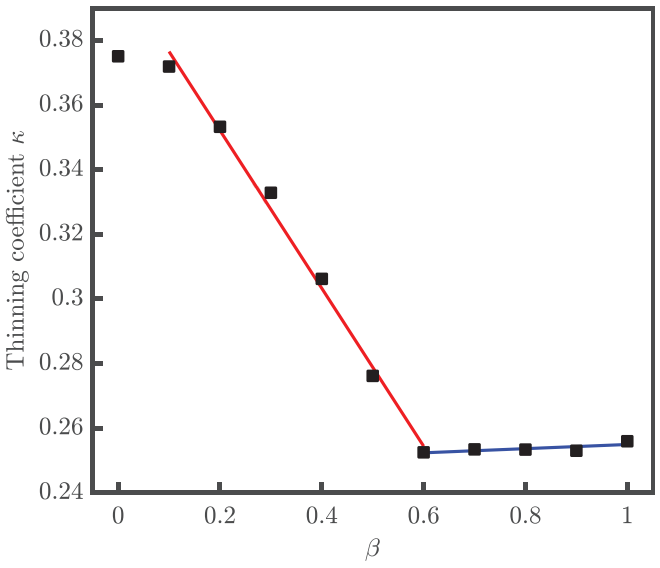


FIG. 11. Coefficient of thinning $\kappa = R^{3/2}/\tau$ for the break-off of the head-drop for different surfactant strengths. Two distinct regimes are shown: before $\beta = 0.6$ where κ decays linearly with β and after $\beta = 0.6$ where κ is almost independent of β.

© Author(s) 2021

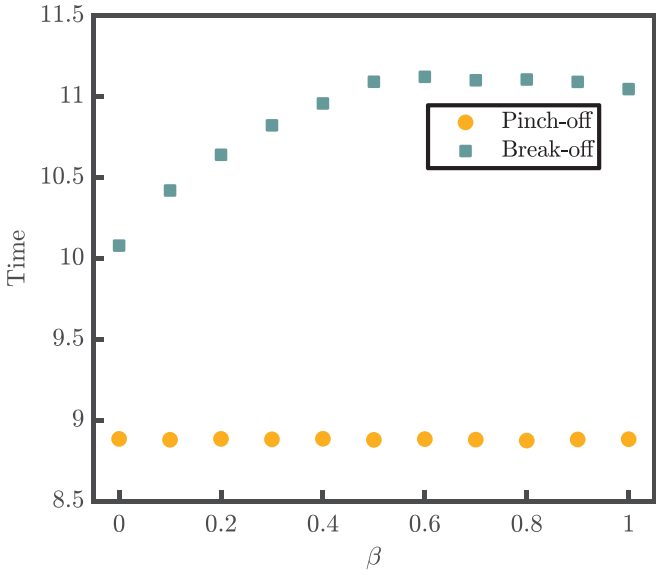


FIG. 12. Dimensionless times for pinch-off from the nozzle and capillary break-off for different surfactant strengths β at $Re = 100$ and $We = 5.56$. The pinch-off time is not affected by the presence of surfactants, whereas the break-off time increases with surfactant strength until a critical value of $\beta = 0.6$.

equation of state, Eq. (33) shown in Fig. 4, where the effect of the surfactant on the surface tension saturates once the surface tension has been reduced to $\gamma_{\min}$ and occurs at lower values of C for larger values of β.

C. Jetting behavior

We now turn our focus to the jetting behavior of the surfactant solutions. We measure different jetting properties, such as the drop speed and the times of the pinch-off from the nozzle and the break-off of the main droplet from the ligament in the case of satellite formation.

For a fixed jetting speed, there is a small increase in the droplet speed of 10%, as the surfactant strength is increased from $\beta = 0$ to $\beta = 0.1$. This is confirmed by our experimental observations. As noted earlier, the pinch-off time is not affected by the presence of the surfactants (Fig. 12). Since the droplet speed and the pinch-off time are barely affected by the surfactants, there is no change to the ligament length.

Even though the surfactants show no effect on most stages of the jetting process, there is an effect on the capillary break-off time. Unlike pinch-off time, the capillary break-off time as shown in Fig. 12 increases with surfactant strength, delaying the capillary break-off event. As with change to the thinning rate (Fig. 11), this increase saturates above the critical value of $\beta = 0.6$, beyond this the strength of the surfactant does not affect the break-off time.

Figure 13(a) compares the free-surface position of pure water and surfactant solutions of different strengths at time $t = 9t_R$, just after the break-off from the nozzle, where the surfactant distribution is similar to that shown in Fig. 8(b). The shape and position of the ligament are unaffected by the presence of the surfactant with the main differences being in position of the head drop, due to the increase in

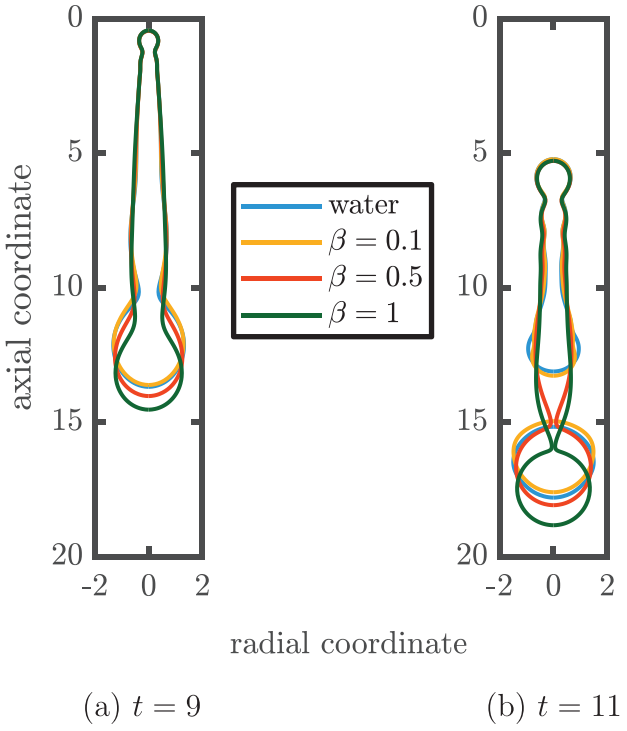


FIG. 13. Surface shape at $t = 9t_R$ and $t = 11t_R$ for different surfactant strengths after pinch-off from the nozzle. (a) At this early stage, the influence of surfactants is negligible, with no significant change on the free surface or in velocity as mentioned earlier. (b) In the pure solution and weak surfactant solution ($\beta = 0.1$), the main droplet has already broken off from the ligament, while at $\beta = 0.5$ it remains attached. A slight increase in the drop speed is noticed particularly for the strongest surfactant $\beta = 1$.

droplet speed with increasing surfactant strength and a reduction in the width of the neck between the ligament and the main drop.

Figure 13(b) shows the surface shape at $t = 11t_R$, corresponding to the time shown in Fig. 9(a). The main drop has already broken-off for the pure water and weaker surfactant solutions, but is still attached for $\beta \geq 0.5$ due to the delay in the break-off time with surfactant strength (Fig. 12).

D. Effect of jetting speed

So far, we have only considered a single Reynolds and Weber number, corresponding to jetting with the same drive amplitude, but with the addition of surfactants of different strengths. In Fig. 14, we consider how the break-up is affected by changing the drive amplitude, which corresponds to varying the Reynolds number, while keeping the Ohnesorge number fixed. The middle figure corresponds to the case $Re = 100$ discussed above, with the shapes of the free surface compared at time $t = 11t_R$. As might be expected, the main difference between the $Re = 200$ and $Re = 100$ cases is the increase in the ligament length, corresponding to the increase in droplet speed. However, the rear sections of the ligaments are almost identical, and the differences at the front of the ligament are due to the slightly later break-off. At the lowest Reynolds number, which corresponds to a Weber

© Author(s) 2021

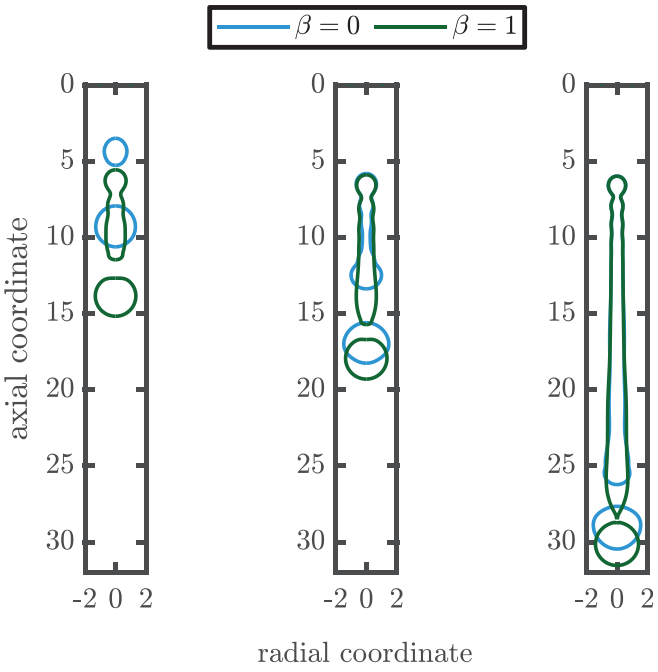


FIG. 14. Surface shape at $t = 11t_R$ for different velocities (from left to right) corresponding to $We = 1.39$, 5.56, 22.22, $Re = 50$, 100, 200, and $Oh = 0.024$.

number of 1.39, the addition of surfactant makes a more significant difference to the drop speed as it reduces the resistance to jetting from surface tension. However in all the cases shown, the presence of surfactant is not able to prevent break-off of the droplet from the ligament, in contrast to the prevention of end-pinching.[26,27]

There are circumstances where the addition of surfactant can prevent break-off from occurring and hence prevent a satellite drop. However, for this waveform we have only found this at higher Ohnesorge numbers and at a lower Weber number. Figure 15 shows the effect of increasing Ohnesorge number from 0.05 to 0.16 by increasing fluid viscosity, at a Weber number of 0.68. At $Oh = 0.16$, the pure fluid produces a satellite drop; however, the addition of a strong surfactant ($\beta = 1$) prevents the capillary break-off so that the ligament is absorbed within the main drop in a similar manner to the escape from end-pinching.[26,27]

As well as delaying capillary break-off Marangoni stresses also modify the flow patterns inside the main droplet. In Fig. 16, the flow relative to the mean velocity is visualized inside droplets with different surfactant strengths just before the capillary break-off. In the pure water case, the flow shows a recirculation within the droplet with a return flow along the surface toward the neck. The addition of surfactants acts to "rigidify" the surface leading to a reduction in the recirculation on the sides with the flow becoming more concentrated along the axis.

VI. CONCLUSIONS

In this paper, we have considered how the presence of surfactants affects jetting and drop formation in inkjet printing. The flow and surface expansion rates associated with the jetting process are much higher than typical timescales of surface diffusion and surface adsorption of

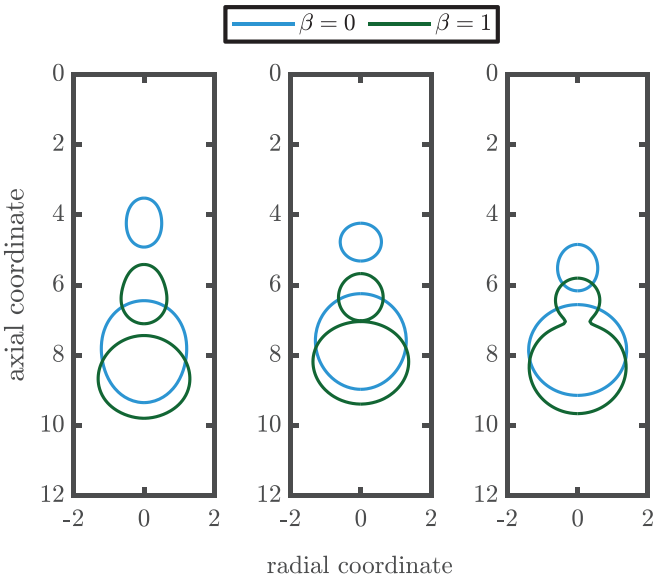


FIG. 15. Surface shape at $t = 12t_R$ for fluids with different viscosities (from left to right), corresponding to $Oh = 0.05$, 0.09, 0.16, $Re = 17.5$, 8.75, 5, and $We = 0.68$. With increasing viscosity and the addition of a strong surfactant ($\beta = 1$), we can prevent the formation of a satellite and have a single droplet as a result.

surfactants. Consequently, surfactants are unevenly distributed with a higher concentration on the surface of the drop compared to the ligament. This gives rise to quite different behavior at the two main break-off events, which are potentially beneficial for inkjet printing.

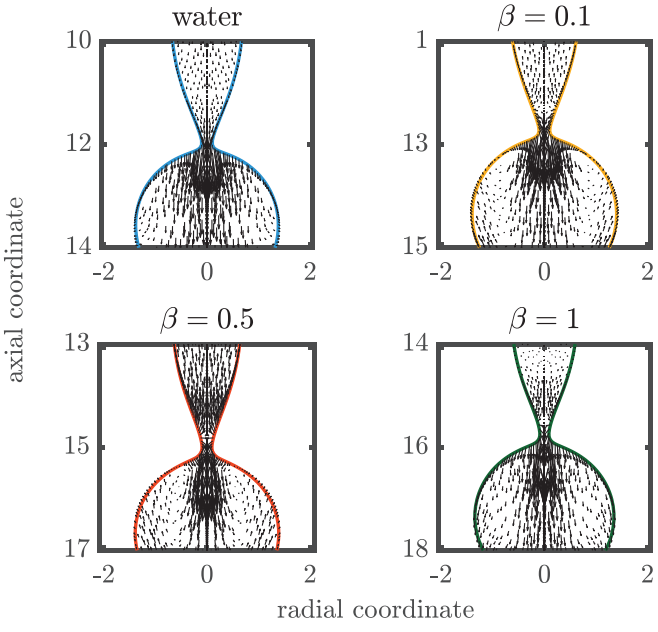


FIG. 16. Flow relative to the mean velocity inside the droplet normalized by the head drop speed for pure water and for water with different surfactant strengths. The times for each of these graphs is different and is chosen as the point just before the capillary break-off.

© Author(s) 2021

1. The absence of surfactants in the vicinity of the break-off at the nozzle exit means that the break-off event follows that of the pure fluid with a high surface tension. This acts to minimize the break-off time and hence the length of the ligament.
2. There is a strong Marangoni stress at the neck between the head drop and the ligament, where the side close to the ligament is surfactant-free and the side of the droplet head has a higher surfactant concentration. Therefore, the break-off time of the main drop from the ligament is delayed, and in some circumstances, we have shown that this effect can prevent the formation of satellites.

However, the latter effect requires a strong surfactant and our experimental study found that overall there is little difference in the jetting behavior between the surfactant solution and pure water for a surfactant with strength $\beta = 0.1$, even though the equilibrium surface tension of the surfactant solution is only half that of water.

Although the present study has focused on inkjet printing, where the drop formation is highly controlled, we would expect to find similar behavior for other rapid drop formation processes such as those found in sprays. Here, we focused on a simple surfactant–water system. However, our model could in principle be extended to consider fluids with more complex surface rheology, including surface active polymers and biological fluids containing phospholipids or proteins[59–61] for which dynamic surface tension can be used as a diagnostic tool. In addition to the dilatational interfacial elasticity, these fluids also exhibit a surface stress in response to shear that would need to be incorporated into the model through a constitutive equation for the surface stress.

ACKNOWLEDGMENTS

E.A. was supported by the Engineering and Physical Sciences Research Council Centre for Doctoral Training in Fluid Dynamics at the University of Leeds under Grant No. EP/L01615X/1. E.A. would like to thank Ricoh for supporting the project. M.R. and T.S. were supported by an Industrial Partnership Programme of the Netherlands Organisation for Scientific Research (NWO), co-financed by Canon Production Printing Netherlands B.V., University of Twente, and Eindhoven University of Technology. T.S. acknowledges financial support from the Max-Planck Centre.

DATA AVAILABILITY

The data that support the findings of this study are available from the corresponding author upon reasonable request.

REFERENCES

[1]Berg, *An Introduction to Interfaces & Colloids: The Bridge to Nanoscience* (World Scientific, 2010).
[2]J. N. Israelachvili, *Intermolecular and Surface Forces* (Academic Press, 2011).
[3]D. Quéré, "Fluid coating on a fiber," Annu. Rev. Fluid Mech. **31**, 347–384 (1999).
[4]A. Q. Shen, B. Gleason, G. H. McKinley, and H. A. Stone, "Fiber coating with surfactant solutions," Phys. Fluids **14**, 4055–4068 (2002).
[5]B. Scheid, J. Delacotte, B. Dollet, E. Rio, F. Restagno, E. Van Nierop, I. Cantat, D. Langevin, and H. A. Stone, "The role of surface rheology in liquid film formation," Europhys. Lett. **90**, 24002 (2010).
[6]J. Lucassen and R. S. Hansen, "Damping of waves on monolayer-covered surfaces: I. Systems with negligible surface dilational viscosity," J. Colloid Interface Sci. **22**, 32–44 (1966).
[7]S. Troian, E. Herbolzheimer, and S. Safran, "Model for the fingering instability of spreading surfactant drops," Phys. Rev. Lett. **65**, 333 (1990).
[8]A. A. Darhuber and S. M. Troian, "Principles of microfluidic actuation by modulation of surface stresses," Annu. Rev. Fluid Mech. **37**, 425–455 (2005).
[9]T. Segers, L. De Rond, N. de Jong, M. Borden, and M. Versluis, "Stability of monodisperse phospholipid-coated microbubbles formed by flow-focusing at high production rates," Langmuir **32**, 3937–3944 (2016).
[10]S. Cohen-Addad, R. Höhler, and O. Pitois, "Flow in foams and flowing foams," Annu. Rev. Fluid Mech. **45**, 241–267 (2013).
[11]M. J. Rosen and J. T. Kunjappu, *Surfactants and Interfacial Phenomena* (John Wiley & Sons, 2012).
[12]C. D. Eggleton, Y. P. Pawar, and K. J. Stebe, "Insoluble surfactants on a drop in an extensional flow: A generalization of the stagnated surface limit to deforming interfaces," J. Fluid Mech. **385**, 79–99 (1999).
[13]W. Milliken, H. A. Stone, and L. Leal, "The effect of surfactant on the transient motion of Newtonian drops," Phys. Fluids A **5**, 69–79 (1993).
[14]W. J. Milliken and L. G. Leal, "The influence of surfactant on the deformation and breakup of a viscous drop: The effect of surfactant solubility," J. Colloid Interface Sci. **166**, 275–285 (1994).
[15]H. A. Stone and L. G. Leal, "The effects of surfactants on drop deformation and breakup," J. Fluid Mech. **220**, 161–186 (1990).
[16]B. Ambravaneswaran and O. A. Basaran, "Effects of insoluble surfactants on the nonlinear deformation and breakup of stretching liquid bridges," Phys. Fluids **11**, 997–1015 (1999).
[17]Y.-C. Liao, H. J. Subramani, E. I. Franses, and O. A. Basaran, "Effects of soluble surfactants on the deformation and breakup of stretching liquid bridges," Langmuir **20**, 9926–9930 (2004).
[18]Y.-C. Liao, E. I. Franses, and O. A. Basaran, "Deformation and breakup of a stretching liquid bridge covered with an insoluble surfactant monolayer," Phys. Fluids **18**, 022101 (2006).
[19]P. M. Kamat, B. W. Wagoner, S. S. Thete, and O. A. Basaran, "Role of Marangoni stress during breakup of surfactant-covered liquid threads: Reduced rates of thinning and microthread cascades," Phys. Rev. Fluids **3**, 043602 (2018).
[20]A. Martínez-Calvo, J. Rivero-Rodríguez, B. Scheid, and A. Sevilla, "Natural break-up and satellite formation regimes of surfactant-laden liquid threads," J. Fluid Mech. **883**, A35 (2020).
[21]P. T. McGough and O. A. Basaran, "Repeated formation of fluid threads in breakup of a surfactant-covered jet," Phys. Rev. Lett. **96**, 054502 (2006).
[22]A. Kalogirou, "Instability of two-layer film flows due to the interacting effects of surfactants, inertia, and gravity," Phys. Fluids **30**, 030707 (2018).
[23]P. K. Notz, A. U. Chen, and O. A. Basaran, "Satellite drops: Unexpected dynamics and change of scaling during pinch-off," Phys. Fluids **13**, 549–552 (2001).
[24]R. Craster, O. Matar, and D. Papageorgiou, "Pinchoff and satellite formation in surfactant covered viscous threads," Phys. Fluids **14**, 1364–1376 (2002).
[25]M. Roché, M. Aytouna, D. Bonn, and H. Kellay, "Effect of surface tension variations on the pinch-off behavior of small fluid drops in the presence of surfactants," Phys. Rev. Lett. **103**, 264501 (2009).
[26]P. M. Kamat, B. W. Wagoner, A. A. Castrejón-Pita, J. R. Castrejón-Pita, C. R. Anthony, and O. A. Basaran, "Surfactant-driven escape from endpinching during contraction of nearly inviscid filaments," J. Fluid Mech. **899**, A28 (2020).
[27]H. Wee, B. W. Wagoner, V. Garg, P. M. Kamat, and O. A. Basaran, "Pinch-off of a surfactant-covered jet," J. Fluid Mech. **908**, A38 (2021).
[28]J. Robinson, C. Sutton, and G. Reid, "Dilute triton x-100 in water as a reference liquid for hydrometer calibration using Cuckow's method," Measurement **57**, 132–137 (2014).
[29]L. Yang and C. D. Bain, "Liquid jet instability and dynamic surface tension effect on breakup," in *NIP & Digital Fabrication Conference* (Society for Imaging Science and Technology, 2009), Vol. 2009, pp. 79–82.
[30]I. Langmuir, "The adsorption of gases on plane surfaces of glass, mica and platinum," J. Am. Chem. Soc. **40**, 1361–1403 (1918).
[31]C.-H. Chang and E. I. Franses, "Adsorption dynamics of surfactants at the air/water interface: A critical review of mathematical models, data, and mechanisms," Colloids Surf., A **100**, 1–45 (1995).
[32]A. Frumkin, "Electrocapillary curve of higher aliphatic acids and the state equation of the surface layer," Z. Phys. Chem. **116**, 466–470 (1925).

© Author(s) 2021

[33]S. Hoath, G. Martin, R. Castrejón-Pita, and I. Hutchings, "Satellite formation in drop-on-demand printing of polymer solutions," in *NIP & Digital Fabrication Conference* (Society for Imaging Science and Technology, 2007), Vol. 2007, pp. 331–335.
[34]S. D. Hoath, O. G. Harlen, and I. M. Hutchings, "Jetting behavior of polymer solutions in drop-on-demand inkjet printing," J. Rheol. **56**, 1109–1127 (2012).
[35]E. Antonopoulou, O. Harlen, M. Walkley, and N. Kapur, "Jetting behavior in drop-on-demand printing: Laboratory experiments and numerical simulations," Phys. Rev. Fluids **5**, 043603 (2020).
[36]N. J. Alvarez, L. M. Walker, and S. L. Anna, "Diffusion-limited adsorption to a spherical geometry: The impact of curvature and competitive time scales," Phys. Rev. E **82**, 011604 (2010).
[37]L. Scriven and C. Sternling, "The Marangoni effects," Nature **187**, 186–188 (1960).
[38]E. I. Franses, O. A. Basaran, and C.-H. Chang, "Techniques to measure dynamic surface tension," Curr. Opin. Colloid Interface Sci. **1**, 296–303 (1996).
[39]S. Lee, D. H. Kim, and D. Needham, "Equilibrium and dynamic interfacial tension measurements at microscopic interfaces using a micropipet technique. 2. Dynamics of phospholipid monolayer formation and equilibrium tensions at the water-air interface," Langmuir **17**, 5544–5550 (2001).
[40]O. A. Basaran, H. Gao, and P. P. Bhat, "Nonstandard inkjets," Annu. Rev. Fluid Mech. **45**, 85–113 (2013).
[41]J. Eastoe and J. Dalton, "Dynamic surface tension and adsorption mechanisms of surfactants at the air–water interface," Adv. Colloid Interface Sci. **85**, 103–144 (2000).
[42]F. Jin, R. Balasubramaniam, and K. J. Stebe, "Surfactant adsorption to spherical particles: The intrinsic length scale governing the shift from diffusion to kinetic-controlled mass transfer," J. Adhes. **80**, 773–796 (2004).
[43]S.-Y. Lin, K. McKeigue, and C. Maldarelli, "Diffusion-controlled surfactant adsorption studied by pendant drop digitization," AIChE J. **36**, 1785–1795 (1990).
[44]N. F. Morrison and O. G. Harlen, "Viscoelasticity in inkjet printing," Rheol. Acta **49**, 619–632 (2010).
[45]R. Li, N. Ashgriz, S. Chandra, and J. R. Andrews, "Contraction of free liquid ligaments," Am. Inst. Chem. Eng. J. **54**, 3084–3091 (2008).
[46]L. G. Leal, *Laminar Flow and Convective Transport Processes: Scaling Principles and Asymptotic Analysis* (Butterworth-Heinemann Series in Chemical Engineering, 1992).
[47]H. A. Stone, "A simple derivation of the time-dependent convective-diffusion equation for surfactant transport along a deforming interface," Phys. Fluids A **2**, 111–112 (1990).
[48]O. Harlen, J. Rallison, and P. Szabo, "A split Lagrangian-Eulerian method for simulating transient viscoelastic flows," J. Non-Newtonian Fluid Mech. **60**, 81–104 (1995).
[49]P. Gresho and R. Sani, *Incompressible Flow and the Finite Element Method* (John Wiley and Sons, Inc., New York, 1998), Vol. 2.
[50]W. M. Deen, *Analysis of Transport Phenomena* (Oxford University Press, New York, 1998).
[51]H. Westborg and O. Hassager, "Creeping motion of long bubbles and drops in capillary tubes," J. Colloid Interface Sci. **133**, 135–147 (1989).
[52]T. Segers, E. Gaud, M. Versluis, and P. Frinking, "High-precision acoustic measurements of the nonlinear dilatational elasticity of phospholipid coated monodisperse microbubbles," Soft Matter **14**, 9550–9561 (2018).
[53]A. van der Bos, A. Zijlstra, E. Gelderblom, and M. Versluis, "ilif: Illumination by laser-induced fluorescence for single flash imaging on a nanoseconds timescale," Exp. Fluids **51**, 1283–1289 (2011).
[54]J. Eggers, "Universal pinching of 3D axisymmetric free-surface flow," Phys. Rev. Lett. **71**, 3458 (1993).
[55]D. T. Papageorgiou, "On the breakup of viscous liquid threads," Phys. Fluids **7**, 1529–1544 (1995).
[56]R. F. Day, E. J. Hinch, and J. R. Lister, "Self-similar capillary pinchoff of an inviscid fluid," Phys. Rev. Lett. **80**, 704 (1998).
[57]Q. Xu, Y.-C. Liao, and O. A. Basaran, "Can surfactant be present at pinch-off of a liquid filament?," Phys. Rev. Lett. **98**, 054503 (2007).
[58]M.-L. E. Timmermans and J. R. Lister, "The effect of surfactant on the stability of a liquid thread," J. Fluid Mech. **459**, 289–306 (2002).
[59]G. G. Fuller and J. Vermant, "Complex fluid-fluid interfaces: Rheology and structure," Annu. Rev. Chem. Biomol. Eng. **3**, 519–543 (2012).
[60]H. Mohwald, "Phospholipid and phospholipid-protein monolayers at the air/water interface," Annu. Rev. Phys. Chem. **41**, 441–476 (1990).
[61]V. Prasad, S. Koehler, and E. R. Weeks, "Two-particle microrheology of quasi-2D viscous systems," Phys. Rev. Lett. **97**, 176001 (2006).

© Author(s) 2021